Intercorrelated anomalous Hall and spin Hall effect in kagome-lattice Co₃Sn₂S₂-based shandite films

Yong-Chang Lau [1,2,3,*] Junya Ikeda,[1] Kohei Fujiwara [1] Akihiro Ozawa [1] Jiaxin Zheng,[4,2] Takeshi Seki,[1,†]
Kentaro Nomura,[1,5] Liang Du,[4] Quansheng Wu [2,3] Atsushi Tsukazaki,[1,6] and Koki Takanashi[1,6,7]

[1]*Institute for Materials Research, Tohoku University, Sendai 980-8577, Japan*
[2]*Beijing National Laboratory for Condensed Matter Physics, and Institute of Physics, Chinese Academy of Sciences, Beijing 100190, China*
[3]*University of Chinese Academy of Sciences, Beijing 100049, China*
[4]*College of Physics and Technology, Guangxi Normal University, Guilin, Guangxi 541004, China*
[5]*Department of Physics, Kyusyu University, Fukuoka 819-0395, Japan*
[6]*Center for Science and Innovation in Spintronics, Core Research Cluster, Tohoku University, Sendai 980-8577, Japan*
[7]*Advanced Science Research Center, Japan Atomic Energy Agency, Tokai 319-1195, Japan*

Magnetic Weyl semimetals (mWSMs) are characterized by linearly dispersive bands with chiral Weyl node pairs associated with broken time-reversal symmetry. One of the hallmarks of mWSMs is the emergence of large intrinsic anomalous Hall effect. On heating the mWSM above its Curie temperature, the magnetism vanishes while exchange-split Weyl point pairs collapse into doubly degenerate gapped Dirac states. Here, we reveal the attractive potential of these Dirac nodes in paramagnetic state for efficient spin current generation at room temperature via the spin Hall effect. Ni and In are introduced to separately substitute Co and Sn in a prototypal mWSM Co₃Sn₂S₂ shandite film and tune the Fermi level. Composition dependence of spin Hall conductivity for paramagnetic shandite at room temperature resembles that of anomalous Hall conductivity for ferromagnetic shandite at low temperature; exhibiting peak-like dependence centering around the Ni-substituted Co₂Ni₁Sn₂S₂ and undoped Co₃Sn₂S₂ compositions, respectively. The observed spin Hall and anomalous Hall conductivity maxima at different compositions reflect optimum Fermi-level positioning relative to the paramagnetic Dirac and magnetic Weyl states, suggesting the common origin and intercorrelation between the two Hall effects. Our findings highlight a strategy for the quest of spin Hall materials, guided by the abundant experimental anomalous Hall-effect data of ferromagnets in the literature.

I. INTRODUCTION

Nontrivial topology in the band structure of a solid can give rise to large Berry curvature [1,2] acting as an effective magnetic field in real space. This field can deflect the electrons in motion, leading to an intrinsic off-diagonal transport contribution that does not depend on the extrinsic electrons' scattering rate. Typical examples are the anomalous Hall effect (AHE) [3] in ferromagnets and its spin counterpart the spin Hall effect (SHE) [4], leading to transverse charge accumulation and spin accumulation, respectively. The latter often involves nonmagnetic metals with strong spin-orbit coupling and allows generation of a transverse spin current capable of manipulating the magnetization of an adjacent nanomagnet. The resulting spin-orbit torques (SOTs) [5] are promising for applications including nonvolatile memory, magnetic logic, field sensing and neuromorphic computing. Finding material systems that exhibit high charge-to-spin conversion efficiency is a key to realize competitive spin-orbitronic devices with low power consumption.

SHE has thus far only been investigated for a small subset of all the known materials. One primary challenge for probing the SHE is the nonconservative nature of the spin current, thus necessitates material integration into devices of comparable length scale (e.g., the thickness) with the commonly nanometric spin-diffusion length λ [6]. In contrast, owing to its ease of evaluation and prolonged history, the AHE characteristics for many conducting magnetic materials are known and available in the literatures. In view of the very similar origin and scaling relationship for AHE [7] and SHE [8], it is tempting to study the intercorrelation between the two phenomena. The establishment of such an intercorrelation, if it exists, will allow fast screening of new materials with potentially large SHE using the abundant AHE data as a facile indicator, and vice versa. In an earlier theoretical study [9], some Co-based Heusler compounds were suggested to exhibit correlated AHE and SHE, although there is no experimental evidence thus far. More recent theoretical and experimental efforts also failed to demonstrate a strong link between AHE and SHE, in either CoPt alloy [10] or 3d ferromagnetic metals [11]. Different from the trivial electronic bands in conventional 3d

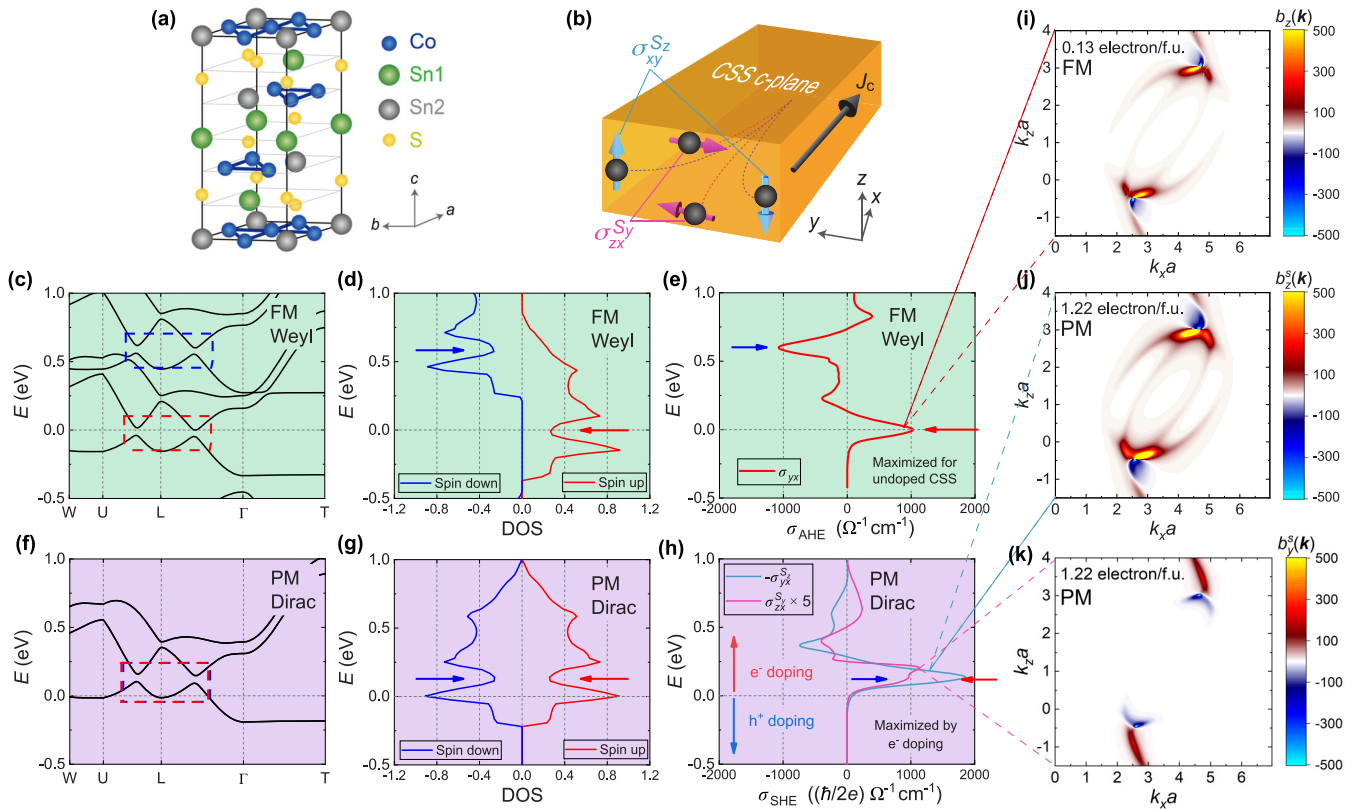*yongchang.lau@iphy.ac.cn
†takeshi.seki@tohoku.ac.jp

FIG. 1. (a) Unit cell of $Co_3Sn_2S_2$ with a Co-kagome lattice in the (*ab*) plane (hexagonal representation). (b) Passing a charge current j_c within the kagome plane along **x** generates, via the spin Hall effect, an orthogonal spin current of conductivity $\sigma_{xy}^{S_z}$ ($\sigma_{zx}^{S_y}$) that flows along **y** (**z**) with polarization along **z** (**y**). Calculated (c) electronic band structure, (d) spin-resolved density of states (DOS), and (e) anomalous Hall conductivity σ_{yx} as a function of Fermi energy for ferromagnetic (FM) $Co_3Sn_2S_2$ in the magnetic Weyl semimetal state. Calculated (f) electronic band structure, (g) spin-resolved DOS, and two selected components $-\sigma_{yx}^{S_z}$ and $\sigma_{zx}^{S_y}$ of the spin Hall conductivity tensor (h) for paramagnetic (PM) $Co_3Sn_2S_2$. $E = 0$ represents the Fermi level E_F for undoped $Co_3Sn_2S_2$ in the FM and PM states. Red and blue dashed boxes in panels (c) and (f) represent the position of the Weyl or Dirac points. The arrows in panels (d)–(h) indicate contributions of these Weyl-Dirac points in DOS and Hall conductivities. (i) Berry curvature distribution $b_z(\mathbf{k})$ and two components of spin Berry curvature distribution (j) $b_z^s(\mathbf{k})$ and (k) $b_y^s(\mathbf{k})$, projected on $k_y = 0$ plane. The Fermi level is adjusted to a doping level of (i) 0.13 electron/f.u. and (j), (k) 1.22 electron/f.u.

ferromagnetic metals [11], here we focus on one of the topological bands in a magnetic Weyl semimetal (mWSM) [12–15] prototype cobalt shandite $Co_3Sn_2S_2$ (CSS) and its substituted alloys to reveal the intriguing correlation between the AHE in the ferromagnetic state and SHE in the paramagnetic state.

Figure 1(a) illustrates a rhombohedral structure of CSS (space group No. 166; $R\bar{3}m$) which consists of alternate Co_3Sn/SnS_2 planes, stacking along the *c*-axis in the hexagonal representation. Co atoms form a kagome lattice within the *ab* plane and exhibit strong perpendicular magnetic anisotropy with Curie temperature (T_C) of ≈ 177 K. Recent spectroscopic studies [16,17] have established ferromagnetic CSS (FM-CSS) as an exotic mWSM with pairs of Weyl points (WPs) near the Fermi level (E_F), connected by the chiral surface Fermi arcs. The WPs, the gapped nodal ring [18] and other topological features near E_F collectively generate large Berry curvature, leading to a record-high anomalous Hall angle exceeding 0.2 in FM-CSS [19,20]. The relatively low T_C of CSS, however, hinders the prospect of exploiting its magnetic topological properties for many practical applications.

Few studies were hitherto devoted to explore the usefulness of CSS at room temperature, i.e., when the CSS is in the paramagnetic state (PM-CSS). Across the ferromagnetic-paramagnetic transition at T_C, the magnetic exchange splitting that stabilizes the mWSM state of FM-CSS collapses, resulting in annihilation of the WPs into gapped Dirac points [21,22]. Inherited from FM-CSS, first-principles band-structure calculations of PM-CSS [23] confirmed the presence of interesting band features including the gapped Dirac point, gapped nodal lines, and topological surface states. However, unlike the FM-CSS with topological bands located near E_F, the E_F of PM-CSS is about 0.23 eV below these unoccupied topological states. Although such an energy gap in PM-CSS has been exploited for oxygen evolution reaction [23], concerning electronic transport, we anticipate limited contribution from these bands, even at room temperature. Here, we highlight the essential role of these correlated Weyl and Dirac bands that respectively give rise to large intrinsic AHE in ferromagnetic state and large intrinsic SHE in paramagnetic state. Furthermore, we experimentally demonstrate that Fermi-level tuning via isostructural substitutional alloying is an effective strategy allowing full exploitation of the Dirac

topological features in the band structure of PM-CSS, for efficient spin current generation via SHE at room temperature.

II. EFFECTIVE TIGHT-BINDING MODEL

To elucidate our concept, we consider a two-orbital effective tight-binding model of CSS [24,25]. A longitudinal charge current j_c is applied along **x** in the *ab* kagome plane, as illustrated in Fig. 1(b). The magnetic easy axis of FM-CSS is along **z** coinciding with the **c** axis. We first focus on FM-CSS in the mWSM state, corresponding to Figs. 1(c)–1(e). The WPs and the gapped nodal lines are indicated by the dashed red box in the simplified electronic band structure of half-metallic FM-CSS in Fig. 1(c). These topological band features are located in the vicinity of E_F (represented by $E = 0$) and manifest themselves in the spin-resolved density of states (DOS) [Fig. 1(d)] as a minimum of the majority spin-up DOS. The anomalous Hall conductivity σ_{yx} (AHC) [Fig. 1(e)] exhibits a peak centering around the WPs at E_F. We highlight that at higher energy, a similar σ_{yx} peak of opposite sign appears (blue arrow), which is attributed to the conjugated magnetic WPs and nodal line gap from the spin-down bands [Fig. 1(c); dashed blue box]. We obtain $\sigma_{AHE} \approx 1.0 \times 10^3 \, \Omega^{-1} \, \text{cm}^{-1}$, which agrees with the experiment and first-principles calculations [19].

The calculated properties of PM-CSS are shown in Figs. 1(f)–1(h). In the absence of magnetic exchange, the spin-split bands of FM-CSS tend to merge and become degenerate without strong distortion. Notably, the conjugated WPs annihilate into doubly degenerate gapped Dirac points. These gaps are sufficiently narrow to be neglected at room temperature. The gapped nodal lines nearby also become degenerate as shown by the piled dashed red and blue boxes in Fig. 1(f). Such magnetic Weyl to paramagnetic Dirac topological transition was previously characterized using angle-resolved photoemission spectroscopy [21,22]. The spin-resolved DOS of the two spin channels are equal, as shown in Fig. 1(g). Note that the electrons' filling redistributes and E_F of PM-CSS now falls on the peaks of the DOS, reflecting the ferromagnetic ground state of CSS based on Stoner criterion. σ_{yx} vanishes regardless of the E_F positioning because contributions from the two spins exactly cancel each other, as expected for a paramagnet. In contrast, the spin current is time-reversal invariant, e.g., a spin-up spin current flowing along **y** is equivalent to a spin-down spin current flowing along −**y**. The spin Berry curvature contributions from the two spin channels are additive and linked to the relative position of the gapped Dirac point and E_F.

We define the spin Hall conductivity (SHC) $\sigma_{ji}^{S_k}$ (i, j, k = x, y, z) where i, j, and k denote the direction of the charge current flow, the spin current flow, and that of the spin-polarization vector, respectively. We consider the common geometry of the SHE in a paramagnet, where the three vectors are orthogonal to each other. As depicted in Fig. 1(b), passing j_c along the **x** axis of PM-CSS generates a lateral spin current (electrons with sky-blue spins) flowing along **y** with polarization along **z** and an out-of-plane spin current (electrons with pink spins) flowing along **z** with transverse spin polarization along **y**. Lateral SHC $-\sigma_{yx}^{S_z}$ [Fig. 1(h); sky-blue line] of approximately twice-as-large

to AHC is expected for E_F located near the gapped Dirac point. We obtain $\sigma_{SHE} \approx 1.9 \times 10^3 (\hbar/2e) \, \Omega^{-1} \, \text{cm}^{-1}$, which approaches that of a typical spin Hall metal Pt [26,27]. In practice, for (0001)-textured CSS film in this work, it is more convenient to detect the out-of-plane spin current with polarization along **y**, i.e., $\sigma_{zx}^{S_y}$. Calculations suggest a peak near the gapped Dirac point for $\sigma_{zx}^{S_y}$ [Fig. 1(h); pink line]. This maximum is however smaller than that of $\sigma_{xy}^{S_z}$ where charge and spin currents are both flowing in the kagome plane, a feature resembles another kagome semimetal Fe_3Sn_2 with highly anisotropic AHC tensor [28]. The strong anisotropy reflects the interplay between the conduction electron, kagome lattice, and spin-orbit coupling, which are essential ingredients for determining the Hall effects.

To confirm the *common* origin of the enhanced Hall conductivities near the Weyl or Dirac points and the nodal lines, we plot in Fig. 1(i) the projection on $k_y = 0$ plane, the Berry curvature distribution $b_z(\boldsymbol{k})$ that contributes to σ_{yx} for FM-CSS with a doping level of 0.13 electron/f.u. Figures 1(j) and 1(k) show the projection on the same plane in momentum space, for PM-CSS with a doping level of 1.22 electron/f.u., the spin Berry curvature distribution $b_z^s(\boldsymbol{k})$ and $b_y^s(\boldsymbol{k})$, corresponding to the SHC $\sigma_{xy}^{S_z}$ and $\sigma_{zx}^{S_y}$, respectively. The very similar Berry and spin Berry curvature hotspots shown in these figures indeed coincide with the position of the magnetic WPs (for FM-CSS) and the gapped Dirac states (for PM-CSS) in momentum space. This scenario is supported by our first-principles calculations on Ni-substituted CSS of various doping, which demonstrate the tunability of Fermi level with respect to the topological bands and the associated AHE and SHE in electron-doped CSS-based shandite compounds. Details will be presented in the Appendix.

Based on these theoretical analysis and in view of the large AHE found in FM-CSS, one can anticipate finding large SHE in electron-doped PM-CSS by experimentally engineering the Fermi level. In the following sections, we present experimental evidences of such Fermi level tuning in In- and Ni-substituted CSS films. We obtain an optimum SHC at room temperature for paramagnetic $Co_2Ni_1Sn_2S_2$ that corroborates the results of the effective-band model and first-principles calculations.

III. EXPERIMENTAL RESULTS

A. Structural characterization

Recently, hole-doped CSS thin flakes of high quality grown by chemical vapor transport method were found to exhibit exceptionally high carrier mobility and low residual resistivity [29]. However, systematic control of the doping level using this method has yet to be achieved and the underlying mechanism of doping remains unclear. On the other hand, the effects of elemental substitution using Fe [30], Ni [31,32], and In [18,33] as dopants have been extensively studied in bulk CSS single crystals, demonstrating the effectiveness of this strategy for tailoring the Fermi level. Theoretical calculations suggest the main features of the CSS electronic band structure remain mostly intact for doping level as high as 1 carrier/f.u. using In [34] and Ni [31] as dopants. Here, we
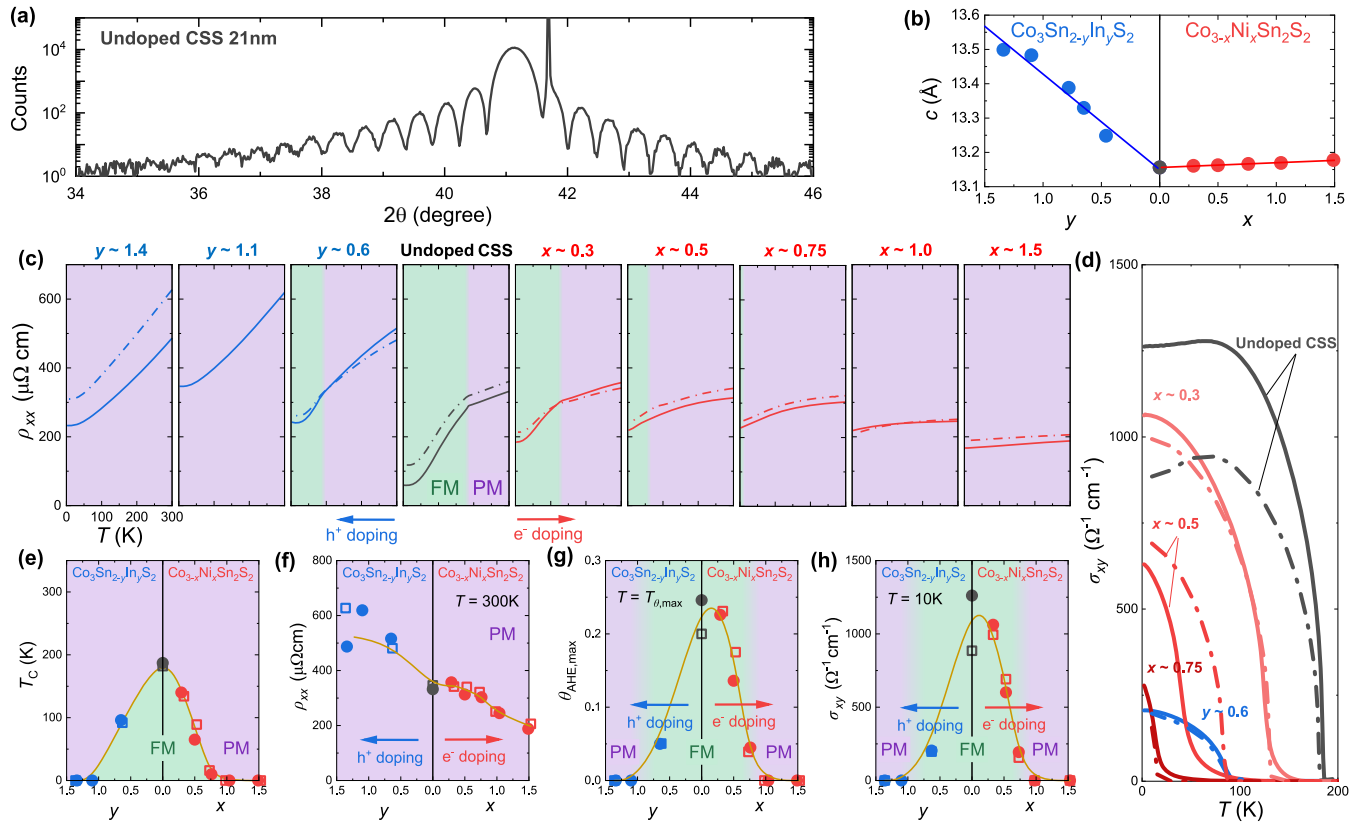
FIG. 2. (a) Typical x-ray diffraction spectrum for an undoped $Co_3Sn_2S_2$ shandite film showing clear Laué fringes near the $Co_3Sn_2S_2(0006)$ reflection. (b) Ni composition x and In composition y dependence of out-of-plane lattice parameter c deduced from the peak position of the (0006) reflection. Temperature T dependence of the (c) longitudinal resistivity ρ_{xx} and (d) anomalous Hall conductivity σ_{xy} for shandite films of various x and y. Solid and dashed lines represent data for the films before and after removing the thick SiO_x capping, respectively. x and y dependence of (e) the Curie temperature T_C, (f) ρ_{xx} at $T = 300$ K, (g) the maximum anomalous Hall angle $\theta_{AHE,max} \equiv \sigma_{xy}\rho_{xx}$ extracted at $T = T_{\theta,max}$, and (h) σ_{xy} at 10 K. Solid and open symbols denote data for shandite films before and after removing the thick SiO_x capping, respectively. Dark yellow solid lines are drawn as guides to the eye.

adopt the second approach and demonstrate systematic tuning of the properties in CSS-based shandite-structured films grown by magnetron co-sputtering. We have grown textured undoped CSS, Ni-substituted $Co_{3-x}Ni_xSn_2S_2$ (CNSS), and In-substituted $Co_3Sn_{2-y}In_yS_2$ (CSIS) films with thicknesses ranging from 11 to 40 nm on Al_2O_3 (0001) substrates, as described previously and in Sec. S1 of the Supplemental Material [25,35–37]. x and y denote the composition of Ni and In, respectively. Upon replacing Co with Ni (Sn with In), the electron (hole) doping is expected to shift E_F to higher (lower) energies. The crystal structure of CSS is maintained throughout because CSS, $Ni_3Sn_2S_2$ and $Co_3In_2S_2$ are isostructural compounds. Figure 2(a) shows typical x-ray diffraction (XRD) spectrum for an undoped CSS film exhibiting clear Laué fringes around the CSS (0006) reflection, indicative of strong (0001) texture with sharp interfaces. In-plane XRD Φ scan of the CSS ($11\bar{2}0$) reflection, however, shows peaks that are $30°$ apart, reflecting the presence of in-plane twinned domains. The out-of-plane lattice parameter c shown in Fig. 2(b) was extracted from the (0006) Bragg peak position for a series of CSS, CNSS, and CSIS films, suggesting systematic tuning of c on varying x and y.

B. Magnetotransport properties

The magnetotransport as a function of temperature T in Figs. 2(c) and 2(d) provides another evidence of systematic tuning of film properties notably in the ferromagnetic state by alloying. Solid lines denote data for undoped CSS (black), CNSS (red), and CSIS (blue) films covered by a thick ≈ 75 nm SiO_x protective layer, whereas dashed lines represent the data for samples after removing the SiO_x layer by Ar ion milling followed by the deposition of 3 nm AlO_x capping [25]. The high quality of our undoped CSS film gives rise to a residual resistivity ratio, RRR $\equiv \rho_{xx}(T = 300$ K$)/\rho_{xx}(T = 10$ K$) \approx 3$. σ_{xy} [Fig. 2(d)] is nearly a plateau for T sufficiently far below T_C, suggesting the dominant intrinsic nature of the AHE in this sample. Meanwhile, for doped films, the kink in $\rho_{xx}(T)$ reflecting T_C and the average resistance are systematically controlled by In and Ni contents. Due to the reduced RRR and T_C with the increase of doping level (hence shrinking the temperature range where the saturation magnetization is roughly a constant), the analyses based on the AHE scaling for extracting the extrinsic skew scattering contribution, if any, become less reliable. More discussions can be found in Sec. IV. T_C, ρ_{xx} at $T = 300$ K, the maximum anomalous
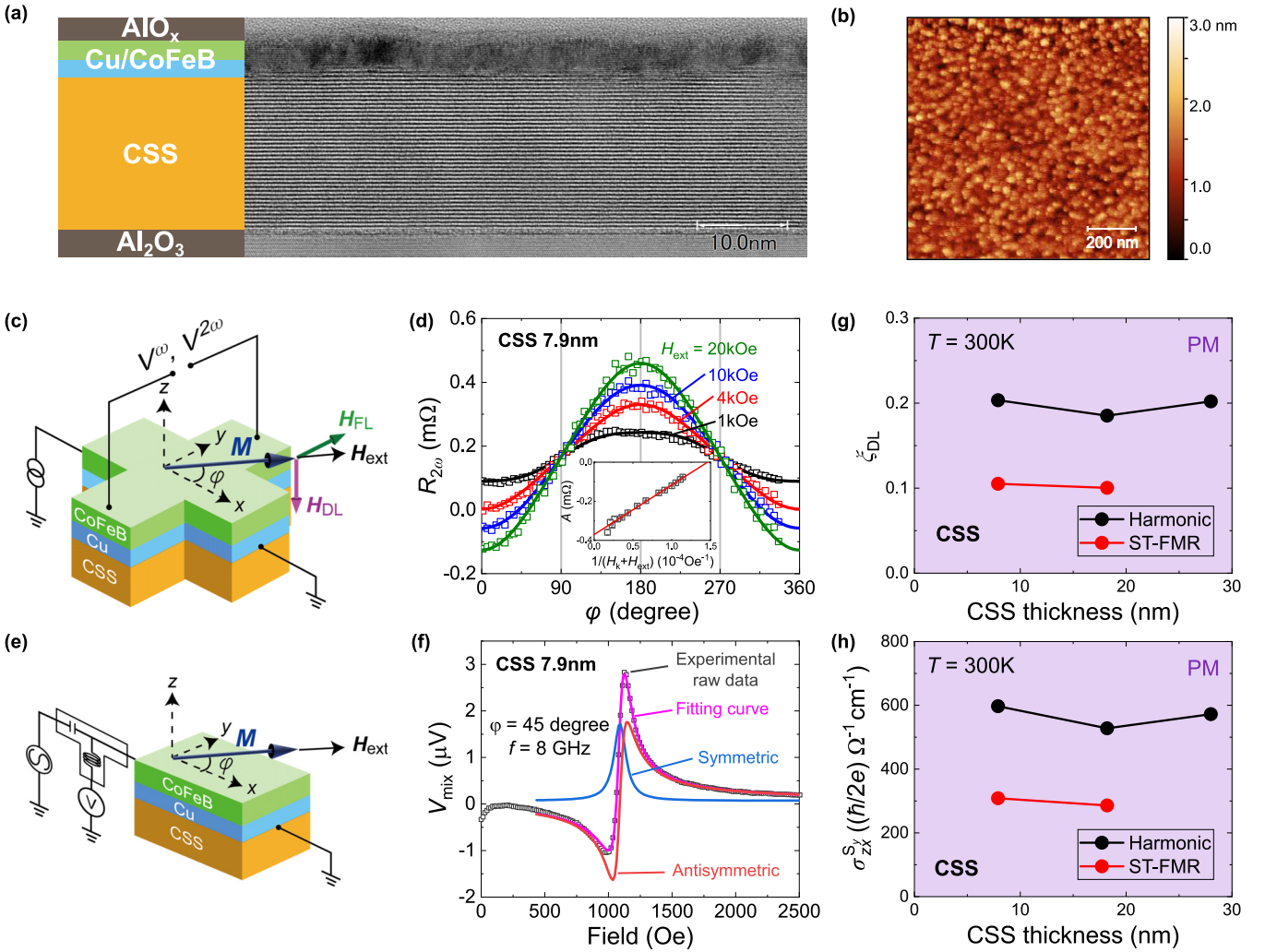
FIG. 3. (a) A schematic of the stack structure and high-resolution cross sectional transmission electron microscopy image for a trilayer with $Co_3Sn_2S_2$ (CSS) thickness $t = 18.5$ nm. (b) Atomic force microscopy image for a trilayer with $t = 7.9$ nm, showing a low root mean square roughness of ≈ 0.3 nm. (c)–(f) Spin-orbit torque quantification of CSS(7.9)/Cu/CoFeB trilayers at $T = 300$ K. (c) Schematic illustration of the harmonic Hall measurement set-up and (d) azimuthal field angle φ dependence of the second-harmonic Hall resistance $R_{2\omega}$ measured at various external fields H_{ext}. The inset of (d) plots A, the prefactor of the $\cos\varphi$ term of $R_{2\omega}$ against the inverse of the effective field $1/(H_k + H_{ext})$. The red line is the best linear fit to the data. (e) Schematic illustration of the spin-torque ferromagnetic resonance (ST-FMR) measurement set-up and (f) a typical FMR spectrum measured at 8 GHz with an applied field along $\varphi = 45°$. The fit and decomposition of the spectrum are based on the sum of a symmetric and an antisymmetric Lorentzian [25]. t dependence of (g) the damping-like spin Hall efficiency ξ_{DL} and (h) spin Hall conductivity $\sigma_{zx}^{S_y}$.

Hall angle $\theta_{AHE,max} \equiv \sigma_{xy}\rho_{xx}$ at $T = T_{\theta,max}$, and σ_{xy} at 10 K are summarized in Figs. 2(e)–2(h). Referring to Stoner criterion, both electron and hole doping reduce T_C because E_F of undoped PM-CSS falls on a local maximum of the DOS [Fig. 1(g)]. Similarly, σ_{xy} at 10 K and $\theta_{AHE,max}$ are maximized for undoped FM-CSS and fall rapidly with increasing x and y. These observations confirm the correlation between the large intrinsic σ_{xy} and the E_F positioning relative to the magnetic WPs and the gapped nodal lines.

C. Spin-orbit torque quantification

We next fabricate undoped CSS(t)/Cu(1.8)/CoFeB(2) (thicknesses in nanometer) trilayers (see Supplemental Material [25]) for investigating the charge-to-spin conversion at $T = 300$ K, i.e., when CSS is paramagnetic. t denotes

the thickness of the CSS layer. Figure 3(a) shows a typical high-resolution cross-sectional transmission electron microscopy image of CSS(18.5)/Cu(1.8)/CoFeB(2) trilayer where the layered structure of high-quality CSS is clearly visible. The average grain size of CSS (>50 nm) is significantly larger than that of Cu/CoFeB (≈ 10 nm). Energy dispersive x-ray spectroscopy mapping confirms that all layers of the heterostructure are continuous with limited interdiffusion (see Fig. S1 in Supplemental Material [25]). Typical atomic force microscopy (AFM) micrograph [Fig. 3(b)] of the trilayer for $t = 7.9$ nm reveals flat surface morphology with a low root mean square surface roughness of ≈ 0.3 nm, which is a prerequisite for spintronic device integration in the future.

On passing a charge current along **x**, PM-CSS generates a spin current flowing along **z** that traverses the Cu spacer and exerts SOTs on the CoFeB with in-plane

magnetization. Limited by the thin-film geometry, only $\sigma_{zx}^{S_i}$; $i = x, y, z$ are accessible. The thin Cu spacer with long λ physically separates CSS and CoFeB, thus avoiding local enrichment of Co at the interface which may alter the properties of CSS. The observation of $\approx 1\%$ current-in-plane giant magnetoresistance for the trilayer at $T = 50$ K (i.e., when CSS is ferromagnetic) confirms the finite spin transparency across the Cu spacer (see Fig. S2 in Supplemental Material [25]). We first employ the harmonic Hall technique [38,39] to quantify the damping-like and field-like spin-orbit effective fields (H_{DL} and H_{FL}, respectively) acting on the CoFeB magnetization [Fig. 3(c)]. The dependence of second-harmonic Hall resistance $R_{2\omega}$ on the external field H_{ext} and its azimuthal angle φ allows separation of the SOT contribution ($\propto 1/H$) from the parasitic thermoelectric effects [40–42]. Figure 3(d) plots the φ-dependence of $R_{2\omega}$ measured at various H_{ext} for trilayer with $t = 7.9$ nm and a current density flowing in the CSS of $j_{CSS} \sim 1.6 \times 10^6$ A/cm^2. $R_{2\omega}(\varphi)$ is dominated by the $\cos\varphi$ term, defined with a prefactor A. (See Sec. S2 of the Supplemental Material for the detailed analysis of the harmonic Hall measurement [25].) H_{DL} is extracted by linear fitting A against the inverse of the effective in-plane field $1/(H_k + H_{ext})$ [insets of Fig. 3(d)]. We found $H_{DL}/j_{CSS} = 1.4 \times 10^{-6}$ Oe A^{-1} cm^2, corresponding to a DL spin Hall efficiency $\xi_{DL} = (2e/\hbar)(H_{DL}M_s t_{CoFeB}/j_{CSS}) \approx +0.20$ where e is the elementary charge, $\hbar$ is Planck's constant, $M_s = 1200$ emu cm^{-3} is the saturation magnetization, and $t_{CoFeB} = 2$ nm is the CoFeB thickness. ξ_{DL} of undoped PM-CSS is of the same sign as that of Pt. Its absolute magnitude is larger than another mWSM prototype Co$_2$MnGa ($\xi_{DL} \approx -0.07$ in the ferromagnetic state) [43]. With $\rho_{xx} \approx 340$ $\mu\Omega$ cm, we obtained $\sigma_{zx}^{S_y} = \xi_{DL}/\rho_{xx} \approx 600(\hbar/2e)$ Ω^{-1} cm^{-1}.

For an independent verification, we performed spin-torque ferromagnetic resonance (ST-FMR) [set-up depicted in Fig. 3(e)] measurement [44] on microstrips fabricated on the same substrate. A representative FMR spectrum measured from the mixing voltage V_{mix} while applying H_{ext} along $\varphi = 45^\circ$ is shown in Fig. 3(f). The spectrum is fit by the sum of a symmetric and an antisymmetric Lorentzian. More details of the analysis can be found in Sec. S3 of the Supplemental

Material [25]. The emergence of an appreciable symmetric component (blue) confirms the generation of DL-SOT from the undoped PM-CSS at room temperature. Lineshape analysis taking into account current shunting in the Cu spacer yields $\xi_{DL} = +0.11$, which is lower than that obtained from the harmonic Hall technique. This is, however, consistent with a recent systematic analysis that ξ_{DL} obtained using the harmonic Hall method is typically 60% larger than that estimated using ST-FMR technique [45]. The full φ dependence of ST-FMR is a powerful means allowing us to confirm the dominant role of spin current with polarization along **y** [see Fig. S4(a) in Supplemental Material [25]]. Figures 3(g) and 3(h) summarize the CSS thickness t dependence of ξ_{DL} and $\sigma_{zx}^{S_y}$ obtained from the two techniques. The almost constant trend of ξ_{DL} and $\sigma_{zx}^{S_y}$ against t for undoped PM-CSS is consistent with the bulk-like SHE picture and λ being much shorter than $t = 7.9$ nm. We consider this upper bound estimation of λ for undoped CSS remains valid for Ni- and In-substituted CSS in the following paragraphs because alloying typically reduces RRR and λ.

We now extend the harmonic Hall SOT quantification at $T = 300$ K to Ni-substituted and In-substituted CSS/Cu/CoFeB trilayers. Substituted CSS layers of thicknesses higher than 15 nm are chosen to minimize potential interference between SOT performance and the reduced film quality due to island-like growth mode [36]. Contrary to σ_{xy} that is maximized for undoped FM-CSS, In and Ni substitutions lead to opposite trends in ξ_{DL} and $\sigma_{zx}^{S_y}$. A direct comparison of the raw harmonic Hall data for CNSS($x \approx 1.0$)/Cu/CoFeB trilayer and CSIS($y \approx 0.6$)/Cu/CoFeB trilayer are shown in Fig. S3 in the Supplemental Material [25]. Both ξ_{DL} and $\sigma_{zx}^{S_y}$ [Figs. 4(a) and 4(b)] exhibit a pronounced peak for electron-doped (Ni-doped) PM shandites. The highest $\xi_{DL} = +0.30$ is achieved for PM-Co$_{2.25}$Ni$_{0.75}$Sn$_2$S$_2$ ($x \approx 0.75$), which is comparable to that of β-W [46]. Taking into account the conductivity enhancement on increasing x [Fig. 2(f)], the peak of $\sigma_{zx}^{S_y} \approx 1000(\hbar/2e)$ Ω^{-1} cm^{-1} is shifted to Co$_{2.02}$Ni$_{0.98}$Sn$_2$S$_2$ ($x \approx 1.0$). The prominent peak feature of composition-dependent $\sigma_{zx}^{S_y}$ resembles that expected for a
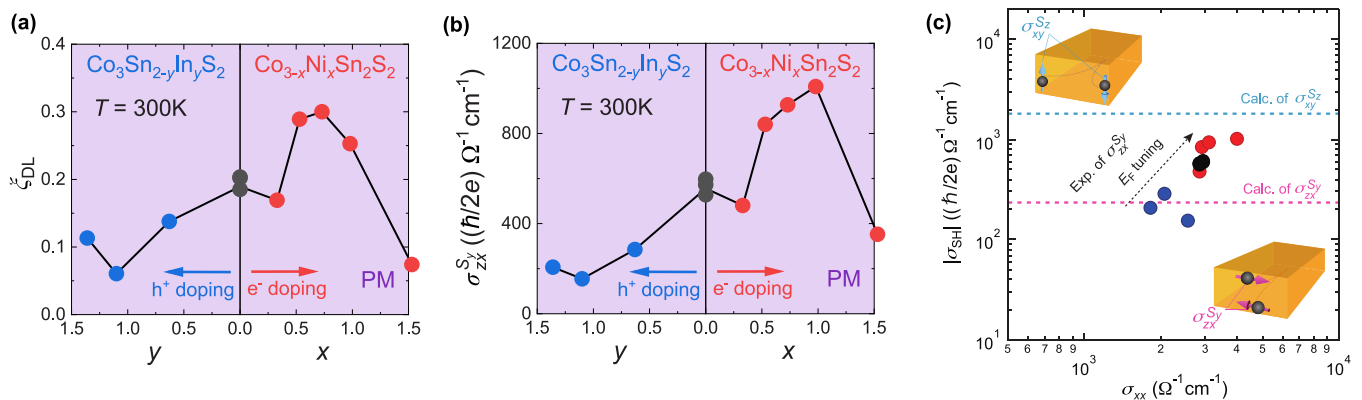

FIG. 4. Nickel (Ni) composition x and Indium (In) composition y dependence of (a) the damping-like spin Hall efficiency ξ_{DL} and (b) spin Hall conductivity $\sigma_{zx}^{S_y}$, for paramagnetic shandites based on the harmonic Hall technique, measured at 300 K. (c) $\sigma_{zx}^{S_y}$ against the longitudinal conductivity σ_{xx} for all the samples. The calculated spin Hall conductivity maxima for $\sigma_{zx}^{S_y}$ and $\sigma_{xy}^{S_z}$ are indicated by the dashed lines with schematics of the spin current geometry in the insets.
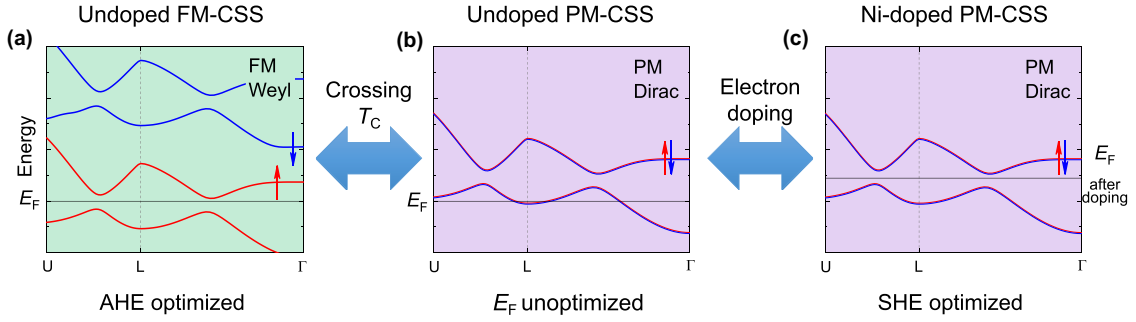
FIG. 5. Illustrations summarizing the evolution of the band structure with spin-orbit coupling and the electrons' filling of CSS at different stages. The AHE in the ferromagnetic state and the SHE in the paramagnetic state depend on the position of the Fermi level E_F from the Weyl or Dirac states. (a) Undoped FM-CSS with E_F near the magnetic Weyl states is optimized for AHE. (b) CSS becomes paramagnetic across T_C. The favorable position of E_F is disrupted. (c) Proper electron doping into PM-CSS is required to reposition E_F near the paramagnetic Dirac states and maximize SHE.

massive Dirac model [18,28] where at the peak composition, E_F cuts a specific band feature (the gapped Dirac states for PM-CSS) providing large spin Berry curvature contribution related to $\sigma_{zx}^{S_y}$. Changing the composition shifts E_F away from the optimum energy level and reduces $\sigma_{zx}^{S_y}$. This model is fully consistent with our observations that ξ_{DL} and $\sigma_{zx}^{S_y}$ decrease dramatically upon introducing In for hole doping. Between $x \approx 1.0$ and $x \approx 1.5$, we found the Hall coefficient of PM-CSS at 250 K smoothly reverses its sign to electron-like, suggesting multiband contribution to the transport (see Fig. S6 in Supplemental Material [25]). We infer that over this x range, E_F may have crossed the Dirac points while the excessive Ni substitution (up to 50% Co substitution) may have strongly distorted the electronic band structure. The high tunability of the experimental $\sigma_{zx}^{S_y}$ spanning over a factor of ≈ 5 is plotted against the longitudinal conductivity σ_{xx} and compared with the calculated $\sigma_{zx}^{S_y}$ and $\sigma_{xy}^{S_z}$ maxima [horizontal dashed lines] in Fig. 4(c). We consider misoriented CSS/Cu interface (e.g., due to the damage induced by Ar ion milling) may partly contribute to the experimental $\sigma_{zx}^{S_y}$ that lies between the two theoretical estimations. More interestingly, the highly anisotropic SHC tensor inherit from the CSS kagome lattice may allow further SHC enhancement, provided high-quality shandite films with the **c** axis lying in the film plane can be stabilized.

IV. DISCUSSION

It is worth noting that, for another Weyl material Mn$_3$Sn with noncollinear antiferromagnetic order, AHE [47], time-reversal-odd magnetic SHE [48], giant magnetic field-like torque [49], and zero-field spin-orbit torque switching [50] were systematically studied and demonstrated below the Néel temperature T_N of the material. The noncollinear magnetic octupole of Mn$_3$Sn plays the common crucial role in the observed phenomena. A fundamental difference is that the AHE and the magnetic SHE are time-reversal odd and being controlled by the magnetic octupole whereas the conventional SHE that we have observed here is time-reversal invariant and stems from the spin-degenerate gapped Dirac states with no magnetism involved. Spin current generation in Mn$_3$Sn therefore involves the interesting interplay between the magnetic

SHE and the conventional SHE, for which the details are beyond the scope of this work.

Figure 5 schematically illustrates the step-by-step evolution of the E_F positioning and the electronic band structure with spin-orbit coupling of CSS, starting from the mWSM state optimized for large AHE to Ni-doped PM-CSS optimized for large SHE. The Fermi level tuning scheme presented in Fig. 1 allows us to reveal strong AHE and SHE contributions that separately stem from the magnetic Weyl and paramagnetic Dirac states in CSS-based shandites. The observed giant AHE and SHE share the common intrinsic origin due to the same topological nontrivial band feature (either being spin-split or degenerate), which makes the two Hall effects naturally intercorrelated. This is the main finding of this work.

To consolidate our claim, potential alternative interpretations involving extrinsic contribution to the Hall effects will be discussed in detailed. Starting from the AHE in FM-CSS: Although previous studies reported the synergetic role of extrinsic mechanism for enhancing the AHE in CSS by Ni, In, and Fe doping [18,30,32], we should emphasize that the extrinsic contribution found in these studies is substantial only for low doping concentration <0.2. Since the extrinsic AHE is additive to the intrinsic one, if the former contribution is dominant in our samples with higher doping level, AHC should further enhance with increasing x and y, which disagrees with the experimental composition dependence of AHC, showing a decreasing trend over a broader range of x and y until the ferromagnetism completely vanishes at $x, y \approx 0.8$. We therefore conclude that the extrinsic mechanism alone cannot fully explain the experimental AHE dependence.

Next, we turn to the SHE that is maximized for PM-CNSS with higher Ni contents $x \approx 0.75$ and $x \approx 1.0$, corresponding to 25% and 33% of Co being substituted by Ni. The weak temperature dependence of ρ_{xx} for CNSS precludes reliable experimental separation of the intrinsic and extrinsic contributions. We thus compare this optimum alloying concentration with other reports in the literature. Dominant extrinsic skew scattering contribution to SHE was reported for systems with typically very high longitudinal conductivity (superclean regime) and lower alloying concentration, e.g., in Cu with $<12\%$ Ir impurities [51] and Cu doped with 0.5% Bi [52]. For the Cu-Ir binary-alloy system with higher Ir

concentration ($>12\%$), it was recently shown that the intrinsic mechanism (or side jump) governs the SHE [53]. In addition, based on the reported positive extrinsic contribution to AHE, one may expect positive extrinsic contribution to SHE for both In and Ni doping, which disagrees with our experimental observations that Ni substitution increases SHC while In substitution has the opposite effect. It is also worth noting that the resistivity at 300 K for CNSS with $x = 0.75$ and $x = 1.0$ are around $200\,\mu\Omega\,\mathrm{cm}$, which corresponds to the so-called moderately dirty conduction regime where intrinsic SHE is expected to be dominant [8]. Extrinsic SHE due to spin-cluster scattering [54,55] can also be safely ruled out because the CNSS neither exhibits strong field-dependent SHC (or otherwise the harmonic Hall quantification will not work) nor does it host magnetic frustration at room temperature enabling spin-chirality scattering. Based on the above arguments, we consider extrinsic mechanisms are unlikely to be responsible for the observed SHC peak for CNSS with $x \approx 1.0$.

Having established the central role of intrinsic mechanism that governs the AHE and SHE in cobalt shandites, we are now in a position to discuss the degree of intercorrelation between the two Hall effects. Tung *et al.* [9] theoretically showed that the anomalous Hall current for many ferromagnetic Co-based full Heusler compounds is almost fully spin polarized, giving rise to correlated AHC and SHC of comparable magnitude (note that the definition of SHC in their work and here differs by a factor of two). This analysis is, however, only valid for material systems with moderate spin-orbit coupling and negligible spin-flip because spin-up and spin-down states tend to be mixed up when the spin-orbit coupling is strong. Ordered CoPt alloy is an example showing little link between the AHC and SHC in ferromagnetic state, owing to the opposite spin character of the band anticrossing at E_F [10] and perhaps the high spin-orbit coupling. Previous calculations have shown that, in ordered FePt alloy, this spin-flip term is greatly reduced upon replacing Pt by Pd [56]. We then consider CSS with Sn being the heaviest constituent at the same row of the periodic table with Pd may also exhibit negligible spin-flip. Combining with the half metallicity of the FM-CSS in the mWSM state (the Weyl points and gapped nodal lines are essentially of the same spin character), CSS system fulfills all basic requirements to show intercorrelated AHE and SHE. In addition, in the paramagnetic state, the conjugated magnetic Weyl features of FM-CSS annihilate to form gapped Dirac states, resulting in further enhancement of the SHC in Ni-doped PM-CSS by doping-controlled Fermi-level tuning. Our experimental results support this scenario and highlight the qualitative correlation between AHE, SHE and the position of E_F from the topological band features.

V. CONCLUSION AND PERSPECTIVE

Compared with the AHE that can be easily measured for a slab-shaped ferromagnetic sample of any size, observation and quantification of SHE is far more challenging, rendering its vast screening laborious and unrealistic. Here, we have demonstrated a strategy where the large intrinsic AHE of a ferromagnetic material may serve as a facile indicator for predicting new paramagnetic compounds with potentially enhanced intrinsic SHE. This rule of thumb is best applied to

ferromagnets where contribution from one spin channel dominates its intrinsic AHE and Berry curvature, as exemplified by the half-metallic mWSM $Co_3Sn_2S_2$. Another prototypal mWSM Co_2MnGa [57] belonging to the highly tunable full Heusler family [58] may also work, provided a proper dopant that simultaneously introduces additional electrons and reduces T_C can be identified. Reciprocally, introducing a ferromagnetic hole dopant into well-established paramagnetic spin Hall materials may lead to the discovery of new ferromagnets with large AHC. This may explain the recent demonstration of large AHC in $L1_2$-ordered $CrPt_3$ compound [59]. One should however be cautious in view of the metallic nature of these materials and the strong spin-orbit coupling of Pt. As a final remark, this strategy is readily extendable to the material screening for thermoelectric generation via the anomalous Nernst effect [60–62] and spin Nernst effect [63,64], provided in addition the Mott relation [65] is satisfied.

APPENDIX: FIRST-PRINCIPLES CALCULATIONS

To check the validity of our effective-band tight-binding model and our interpretation based on rigid-band approximation against In and Ni substitution in paramagnetic CSS, we have also performed first-principles calculations on Ni-doped CSS of various compositions. The calculations are implemented in VASP5.4.4 [66–68], WANNIER90 (v1.2) [69] and WANNIERTOOLS [70]. The cutoff energy for the plane-wave basis [71] set is 400 eV. The projector augmented waves
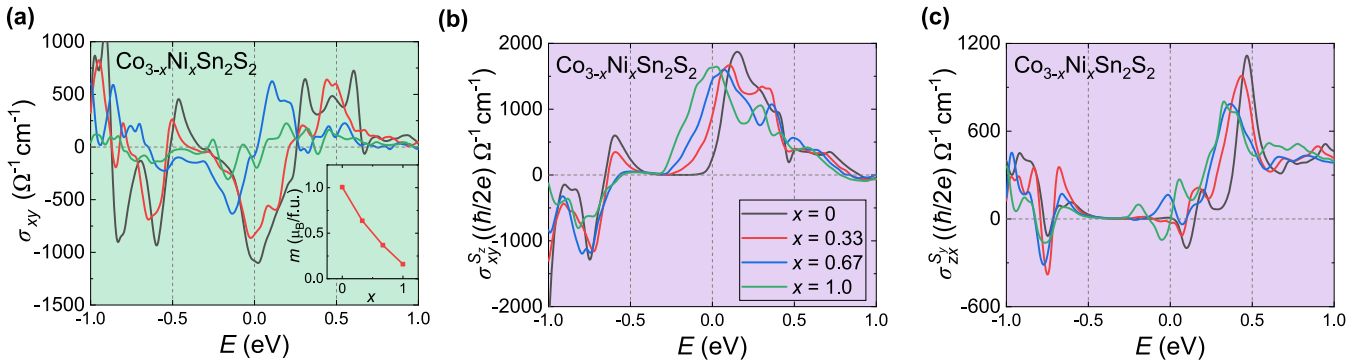
FIG. 6. Calculated intrinsic anomalous Hall conductivity σ_{xy} as a function of the Fermi energy (a) for Ni-doped ferromagnetic CSS of varying compositions x. Inset shows the evolution of the total moment per formula unit m as a function of x. Calculated spin Hall conductivity components (b) $\sigma_{xy}^{S_z}$ and (c) $\sigma_{zx}^{S_y}$ for Ni-doped CSS in the paramagnetic state.

pseudopotential is employed throughout the calculations and spin-orbit coupling is considered in the electronic structure calculations.

A supercell of general formula $Co_{9-i}Ni_iSn_6S_6$ ($i = 0, 1, 2, 3$) is defined, corresponding to Ni concentrations $x = 0, 0.33, 0.67, 1.0$ for $Co_{3-x}Ni_xSn_2S_2$ in experiments. The same calculated lattice constants $a = 5.3689\,\text{Å}$ and $c = 13.176\,\text{Å}$ are used for CNSS without or with Ni doping. When $x = 0$, there are four independent Wyckoff sites: (2/3, 5/6, 5/6) for Co, (1/3, 2/3, z) for S, (0,0,0) for Sn$_1$ and (2/3, 1/3, 5/6) for Sn$_2$, where $z = 0.9503$. The other situations are (2/3, 5/6, 5/6) for Ni when $x = 0.33$, (1/3, 1/6, 1/6) for Ni$_1$ and (0, 1/2, 1/2) for Ni$_2$ when $x = 0.66$, (2/3, 5/6, 5/6) for Ni$_1$, (5/6, 1/6, 1/6) for Ni$_2$ and (1/2, 1/2, 1/2) for Ni$_3$ when $x = 1.00$. With these atomic configurations, we confirm the ferromagnetic ground state for CNSS and systematic evolution of the total moment against x, as shown in the inset of Fig. 6(a).

The k meshes of $50 \times 50 \times 50$ are used to calculate the intrinsic anomalous Hall and spin Hall conductivity. Figure 6(a) plots the calculated intrinsic anomalous Hall conductivity σ_{xy}

against the Fermi energy for ferromagnetic CNSS of varying x. The spin Hall conductivity components $\sigma_{xy}^{S_z}$ and $\sigma_{zx}^{S_y}$ for CNSS in the paramagnetic state are shown in Figs. 6(b) and 6(c), respectively. For AHC in the ferromagnetic state, the σ_{xy} peak deforms and eventually collapses with increasing x, suggesting the varying magnetic exchange due to Ni doping in FM-CSS can violate the rigid-band approximation. In contrast, without this complication, the rigid-band approximation can well describe the systematic shift of the $\sigma_{xy}^{S_z}$ SHC peak as a function of x for electron doping in paramagnetic CSS using Ni substitution up to $x = 1.0$. The calculations also demonstrate strong anisotropy of SHC tensor at the Fermi level (e.g., $\sigma_{xy}^{S_z} \geqslant \sigma_{zx}^{S_y}$), which is attributed to the two-dimensional kagome lattice of CSS. Finally, it is worth mentioning that, although there is an apparent sign conflict between *ab initio* calculations and experiments, we have verified that the calculated AHC for FM-CSS is of the same sign as that of bcc-Fe. The calculated SHC component $\sigma_{xy}^{S_z}$ for PM-CNSS is of the same sign as that of fcc-Pt. These two features are in good agreement with experiments.

[1] M. V. Berry, Quantal phase factors accompanying adiabatic changes, Proc. R. Soc. London, Ser. A **392**, 45 (1984).

[2] D. Xiao, M.-C. Chang, and Q. Niu, Berry phase effects on electronic properties, Rev. Mod. Phys. **82**, 1959 (2010).

[3] N. Nagaosa, J. Sinova, S. Onoda, A. H. MacDonald, and N. P. Ong, Anomalous Hall effect, Rev. Mod. Phys. **82**, 1539 (2010).

[4] J. Sinova, S. O. Valenzuela, J. Wunderlich, C. H. Back, and T. Jungwirth, Spin Hall effects, Rev. Mod. Phys. **87**, 1213 (2015).

[5] A. Manchon, J. Železný, I. M. Miron, T. Jungwirth, J. Sinova, A. Thiaville, K. Garello, and P. Gambardella, Current-induced spin-orbit torques in ferromagnetic and antiferromagnetic systems, Rev. Mod. Phys. **91**, 035004 (2019).

[6] J. Bass and W. P. Pratt, Spin-diffusion lengths in metals and alloys, and spin-flipping at metal/metal interfaces: An experimentalist's critical review, J. Phys.: Condens. Matter **19**, 183201 (2007).

[7] S. Onoda, N. Sugimoto, and N. Nagaosa, Quantum transport theory of anomalous electric, thermoelectric, and thermal Hall effects in ferromagnets, Phys. Rev. B **77**, 165103 (2008).

[8] H. Moriya, A. Musha, S. Haku, and K. Ando, Observation of the crossover between metallic and insulating regimes of the spin Hall effect, Commun. Phys. **5**, 12 (2022).

[9] J.-C. Tung and G.-Y. Guo, High spin polarization of the anomalous Hall current in Co-based Heusler compounds, New J. Phys. **15**, 033014 (2013).

[10] G. Qu, K. Nakamura, and M. Hayashi, First principles investigation of anomalous Hall and spin Hall effects in ferromagnetic copt, J. Phys. Soc. Jpn. **90**, 024707 (2021).

[11] Y. Omori, E. Sagasta, Y. Niimi, M. Gradhand, L. E. Hueso, F. Casanova, and Y. C. Otani, Relation between spin Hall effect and anomalous Hall effect in 3d ferromagnetic metals, Phys. Rev. B **99**, 014403 (2019).

[12] O. Vafek and A. Vishwanath, Dirac fermions in solids: From high-T_c cuprates and graphene to topological insulators and Weyl semimetals, Annu. Rev. Condens. Matter Phys. **5**, 83 (2014).

[13] B. Yan and C. Felser, Topological materials: Weyl semimetals, Annu. Rev. Condens. Matter Phys. **8**, 337 (2017).

[14] N. P. Armitage, E. J. Mele, and A. Vishwanath, Weyl and Dirac semimetals in three-dimensional solids, Rev. Mod. Phys. **90**, 015001 (2018).

[15] N. Nagaosa, T. Morimoto, and Y. Tokura, Transport, magnetic and optical properties of Weyl materials, Nat. Rev. Mater. **5**, 621 (2020).

[16] D. F. Liu, A. J. Liang, E. K. Liu, Q. N. Xu, Y. W. Li, C. Chen, D. Pei, W. J. Shi, S. K. Mo, P. Dudin, T. Kim, C. Cacho, G. Li, Y. Sun, L. X. Yang, Z. K. Liu, S. S. P. Parkin, C. Felser, and Y. L. Chen, Magnetic Weyl semimetal phase in a kagomé crystal, Science **365**, 1282 (2019).

[17] N. Morali, R. Batabyal, P. K. Nag, E. Liu, Q. Xu, Y. Sun, B. Yan, C. Felser, N. Avraham, and H. Beidenkopf, Fermi-arc diversity on surface terminations of the magnetic Weyl semimetal $Co_3Sn_2S_2$, Science **365**, 1286 (2019).

[18] H. Zhou, G. Chang, G. Wang, X. Gui, X. Xu, J.-X. Yin, Z. Guguchia, S. S. Zhang, T.-R. Chang, H. Lin, W. Xie, M. Z. Hasan, and S. Jia, Enhanced anomalous Hall effect in the magnetic topological semimetal $Co_3Sn_{2-x}In_xs_2$, Phys. Rev. B **101**, 125121 (2020).

[19] E. Liu, Y. Sun, N. Kumar, L. Muechler, A. Sun, L. Jiao, S.-Y. Yang, D. Liu, A. Liang, Q. Xu, J. Kroder, V. Süß, H. Borrmann, C. Shekhar, Z. Wang, C. Xi, W. Wang, W. Schnelle, S. Wirth, Y. Chen *et al.*, Giant anomalous Hall effect in a ferromagnetic kagome-lattice semimetal, Nat. Phys. **14**, 1125 (2018).

[20] Q. Wang, Y. Xu, R. Lou, Z. Liu, M. Li, Y. Huang, D. Shen, H. Weng, S. Wang, and H. Lei, Large intrinsic anomalous Hall effect in half-metallic ferromagnet $Co_3Sn_2S_2$ with magnetic Weyl fermions, Nat. Commun. **9**, 3681 (2018).

[21] I. Belopolski, T. A. Cochran, X. Liu, Z.-J. Cheng, X. P. Yang, Z. Guguchia, S. S. Tsirkin, J.-X. Yin, P. Vir, G. S. Thakur, S. S. Zhang, J. Zhang, K. Kaznatcheev, G. Cheng, G. Chang, D. Multer, N. Shumiya, M. Litskevich, E. Vescovo, T. K. Kim *et al.*, Signatures of Weyl Fermion Annihilation in a Correlated Kagome Magnet, Phys. Rev. Lett. **127**, 256403 (2021).

[22] D. F. Liu, Q. N. Xu, E. K. Liu, J. L. Shen, C. C. Le, Y. W. Li, D. Pei, A. J. Liang, P. Dudin, T. K. Kim, C. Cacho, Y. F. Xu, Y. Sun, L. X. Yang, Z. K. Liu, C. Felser, S. S. P. Parkin, and Y. L. Chen, Topological phase transition in a magnetic Weyl semimetal, Phys. Rev. B **104**, 205140 (2021).

[23] G. Li, Q. Xu, W. Shi, C. Fu, L. Jiao, M. E. Kamminga, M. Yu, H. Tüysüz, N. Kumar, V. Süß, R. Saha, A. K. Srivastava, S. Wirth, G. Auffermann, J. Gooth, S. Parkin, Y. Sun, E. Liu, and C. Felser, Surface states in bulk single crystal of topological semimetal $Co_3Sn_2S_2$ toward water oxidation, Sci. Adv. **5**, eaaw9867 (2019).

[24] A. Ozawa and K. Nomura, Two-orbital effective model for magnetic Weyl semimetal in Kagome-lattice shandite, J. Phys. Soc. Jpn. **88**, 123703 (2019).

[25] See Supplemental Material at http://link.aps.org/supplemental/10.1103/PhysRevB.108.064429 for detailed sample preparation, magneto-transport, harmonic Hall technique analysis, spin-torque ferromagnetic resonance analysis, and tight-binding effective-band model calculations.

[26] G. Y. Guo, S. Murakami, T.-W. Chen, and N. Nagaosa, Intrinsic Spin Hall Effect in Platinum: First-Principles Calculations, Phys. Rev. Lett. **100**, 096401 (2008).

[27] A. Hoffmann, Spin Hall effects in metals, IEEE Trans. Magn. **49**, 5172 (2013).

[28] L. Ye, M. Kang, J. Liu, F. von Cube, C. R. Wicker, T. Suzuki, C. Jozwiak, A. Bostwick, E. Rotenberg, D. C. Bell, L. Fu, R. Comin, and J. G. Checkelsky, Massive Dirac fermions in a ferromagnetic kagome metal, Nature (London) **555**, 638 (2018).

[29] M. Tanaka, Y. Fujishiro, M. Mogi, Y. Kaneko, T. Yokosawa, N. Kanazawa, S. Minami, T. Koretsune, R. Arita, S. Tarucha, M. Yamamoto, and Y. Tokura, Topological kagome magnet $Co_3Sn_2S_2$ thin flakes with high electron mobility and large anomalous Hall effect, Nano Lett. **20**, 7476 (2020).

[30] J. Shen, Q. Zeng, S. Zhang, H. Sun, Q. Yao, X. Xi, W. Wang, G. Wu, B. Shen, Q. Liu, and E. Liu, 33% giant anomalous Hall current driven by both intrinsic and extrinsic contributions in magnetic Weyl semimetal $Co_3Sn_2S_2$, Adv. Funct. Mater. **30**, 2000830 (2020).

[31] G. S. Thakur, P. Vir, S. N. Guin, C. Shekhar, R. Weihrich, Y. Sun, N. Kumar, and C. Felser, Intrinsic anomalous Hall effect in Ni-substituted magnetic Weyl semimetal $Co_3Sn_2S_2$, Chem. Mater. **32**, 1612 (2020).

[32] J. Shen, Q. Yao, Q. Zeng, H. Sun, X. Xi, G. Wu, W. Wang, B. Shen, Q. Liu, and E. Liu, Local Disorder-Induced Elevation of Intrinsic Anomalous Hall Conductance in an Electron-Doped Magnetic Weyl Semimetal, Phys. Rev. Lett. **125**, 086602 (2020).

[33] J. Corps, P. Vaqueiro, A. Aziz, R. Grau-Crespo, W. Kockelmann, J.-C. Jumas, and A. V. Powell, Interplay of metal-atom ordering, Fermi level tuning, and thermoelectric properties in cobalt shandites $Co_3M_2S_2$ (M = Sn, In), Chem. Mater. **27**, 3946 (2015).

[34] Y. Yanagi, J. Ikeda, K. Fujiwara, K. Nomura, A. Tsukazaki, and M.-T. Suzuki, First-principles investigation of magnetic and transport properties in hole-doped shandite compounds $Co_3In_xSn_{2-x}S_2$, Phys. Rev. B **103**, 205112 (2021).

[35] K. Fujiwara, J. Ikeda, J. Shiogai, T. Seki, K. Takanashi, and A. Tsukazaki, Ferromagnetic $Co_3Sn_2S_2$ thin films fabricated by co-sputtering, Jpn. J. Appl. Phys. (1962–1981) **58**, 050912 (2019).

[36] J. Ikeda, K. Fujiwara, J. Shiogai, T. Seki, K. Nomura, K. Takanashi, and A. Tsukazaki, Critical thickness for the emergence of Weyl features in $Co_3Sn_2S_2$ thin films, Commun. Mater. **2**, 18 (2021).

[37] J. Ikeda, K. Fujiwara, J. Shiogai, T. Seki, K. Nomura, K. Takanashi, and A. Tsukazaki, Two-dimensionality of metallic surface conduction in $Co_3Sn_2S_2$ thin films, Commun. Phys. **4**, 117 (2021).

[38] J. Kim, J. Sinha, M. Hayashi, M. Yamanouchi, S. Fukami, T. Suzuki, S. Mitani, and H. Ohno, Layer thickness dependence of the current-induced effective field vector in Ta|CoFeB|MgO, Nat. Mater. **12**, 240 (2013).

[39] K. Garello, I. M. Miron, C. O. Avci, F. Freimuth, Y. Mokrousov, S. Blügel, S. Auffret, O. Boulle, G. Gaudin, and P. Gambardella, Symmetry and magnitude of spin-orbit torques in ferromagnetic heterostructures, Nat. Nanotechnol. **8**, 587 (2013).

[40] C. O. Avci, K. Garello, M. Gabureac, A. Ghosh, A. Fuhrer, S. F. Alvarado, and P. Gambardella, Interplay of spin-orbit torque and thermoelectric effects in ferromagnet/normal-metal bilayers, Phys. Rev. B **90**, 224427 (2014).

[41] N. Roschewsky, E. S. Walker, P. Gowtham, S. Muschinske, F. Hellman, S. R. Bank, and S. Salahuddin, Spin-orbit torque and

Nernst effect in Bi-Sb/Co heterostructures, Phys. Rev. B **99**, 195103 (2019).

[42] Z. Chi, Y.-C. Lau, X. Xu, T. Ohkubo, K. Hono, and M. Hayashi, The spin Hall effect of Bi-Sb alloy driven by thermally excited Dirac-like electrons, Sci. Adv. **6**, eaay2324 (2020).

[43] K. Tang, Z. Wen, Y.-C. Lau, H. Sukegawa, T. Seki, and S. Mitani, Magnetization switching induced by spin–orbit torque from Co_2MnGa magnetic Weyl semimetal thin films, Appl. Phys. Lett. **118**, 062402 (2021).

[44] L. Liu, T. Moriyama, D. C. Ralph, and R. A. Buhrman, Spin-Torque Ferromagnetic Resonance Induced by the Spin Hall Effect, Phys. Rev. Lett. **106**, 036601 (2011).

[45] S. Karimeddiny, J. A. Mittelstaedt, R. A. Buhrman, and D. C. Ralph, Transverse and Longitudinal Spin-Torque Ferromagnetic Resonance for Improved Measurement of Spin-Orbit Torque, Phys. Rev. Appl. **14**, 024024 (2020).

[46] C.-F. Pai, L. Liu, Y. Li, H. W. Tseng, D. C. Ralph, and R. A. Buhrman, Spin transfer torque devices utilizing the giant spin Hall effect of tungsten, Appl. Phys. Lett. **101**, 122404 (2012).

[47] S. Nakatsuji, N. Kiyohara, and T. Higo, Large anomalous Hall effect in a non-collinear antiferromagnet at room temperature, Nature (London) **527**, 212 (2015).

[48] M. Kimata, H. Chen, K. Kondou, S. Sugimoto, P. K. Muduli, M. Ikhlas, Y. Omori, T. Tomita, A. H. MacDonald, S. Nakatsuji, and Y. Otani, Magnetic and magnetic inverse spin Hall effects in a non-collinear antiferromagnet, Nature (London) **565**, 627 (2019).

[49] K. Kondou, H. Chen, T. Tomita, M. Ikhlas, T. Higo, A. H. MacDonald, S. Nakatsuji, and Y. Otani, Giant field-like torque by the out-of-plane magnetic spin Hall effect in a topological antiferromagnet, Nat. Commun. **12**, 6491 (2021).

[50] S. Hu, D.-F. Shao, H. Yang, C. Pan, Z. Fu, M. Tang, Y. Yang, W. Fan, S. Zhou, E. Y. Tsymbal, and X. Qiu, Efficient perpendicular magnetization switching by a magnetic spin Hall effect in a noncollinear antiferromagnet, Nat. Commun. **13**, 4447 (2022).

[51] Y. Niimi, M. Morota, D. H. Wei, C. Deranlot, M. Basletic, A. Hamzic, A. Fert, and Y. Otani, Extrinsic Spin Hall Effect Induced by Iridium Impurities in Copper, Phys. Rev. Lett. **106**, 126601 (2011).

[52] Y. Niimi, Y. Kawanishi, D. H. Wei, C. Deranlot, H. X. Yang, M. Chshiev, T. Valet, A. Fert, and Y. Otani, Giant Spin Hall Effect Induced by Skew Scattering from Bismuth Impurities inside Thin Film CuBi Alloys, Phys. Rev. Lett. **109**, 156602 (2012).

[53] H. Masuda, R. Modak, T. Seki, K.-i. Uchida, Y.-C. Lau, Y. Sakuraba, R. Iguchi, and K. Takanashi, Large spin-Hall effect in non-equilibrium binary copper alloys beyond the solubility limit, Commun. Mater. **1**, 75 (2020).

[54] H. Ishizuka and N. Nagaosa, Large anomalous Hall effect and spin Hall effect by spin-cluster scattering in the strong-coupling limit, Phys. Rev. B **103**, 235148 (2021).

[55] Y. Fujishiro, N. Kanazawa, R. Kurihara, H. Ishizuka, T. Hori, F. S. Yasin, X. Yu, A. Tsukazaki, M. Ichikawa, M. Kawasaki, N. Nagaosa, M. Tokunaga, and Y. Tokura, Giant anomalous Hall effect from spin-chirality scattering in a chiral magnet, Nat. Commun. **12**, 317 (2021).

[56] H. Zhang, F. Freimuth, S. Blügel, Y. Mokrousov, and I. Souza, Role of Spin-Flip Transitions in the Anomalous Hall Effect of FePt Alloy, Phys. Rev. Lett. **106**, 117202 (2011).

[57] I. Belopolski, K. Manna, D. S. Sanchez, G. Chang, B. Ernst, J. Yin, S. S. Zhang, T. Cochran, N. Shumiya, H. Zheng, B. Singh, G. Bian, D. Multer, M. Litskevich, X. Zhou, S.-M. Huang, B. Wang, T.-R. Chang, S.-Y. Xu, A. Bansil *et al.*, Discovery of topological Weyl fermion lines and drumhead surface states in a room temperature magnet, Science **365**, 1278 (2019).

[58] K. Manna, L. Muechler, T.-H. Kao, R. Stinshoff, Y. Zhang, J. Gooth, N. Kumar, G. Kreiner, K. Koepernik, R. Car, J. Kübler, G. H. Fecher, C. Shekhar, Y. Sun, and C. Felser, From Colossal to Zero: Controlling the Anomalous Hall Effect in Magnetic Heusler Compounds via Berry Curvature Design, Phys. Rev. X **8**, 041045 (2018).

[59] A. Markou, J. Gayles, E. Derunova, P. Swekis, J. Noky, L. Zhang, M. N. Ali, Y. Sun, and C. Felser, Hard magnet topological semimetals in $X Pt_3$ compounds with the harmony of Berry curvature, Commun. Phys. **4**, 104 (2021).

[60] A. Sakai, S. Minami, T. Koretsune, T. Chen, T. Higo, Y. Wang, T. Nomoto, M. Hirayama, S. Miwa, D. Nishio-Hamane, F. Ishii, R. Arita, and S. Nakatsuji, Iron-based binary ferromagnets for transverse thermoelectric conversion, Nature (London) **581**, 53 (2020).

[61] T. Asaba, V. Ivanov, S. M. Thomas, S. Y. Savrasov, J. D. Thompson, E. D. Bauer, and F. Ronning, Colossal anomalous Nernst effect in a correlated noncentrosymmetric kagome ferromagnet, Sci. Adv. **7**, eabf1467 (2021).

[62] Y. Pan, C. Le, B. He, S. J. Watzman, M. Yao, J. Gooth, J. P. Heremans, Y. Sun, and C. Felser, Giant anomalous Nernst signal in the antiferromagnet $YbMnBi_2$, Nat. Mater. **21**, 203 (2022).

[63] S. Meyer, Y.-T. Chen, S. Wimmer, M. Althammer, T. Wimmer, R. Schlitz, S. Geprägs, H. Huebl, D. Ködderitzsch, H. Ebert, G. E. W. Bauer, R. Gross, and S. T. B. Goennenwein, Observation of the spin Nernst effect, Nat. Mater. **16**, 977 (2017).

[64] P. Sheng, Y. Sakuraba, Y.-C. Lau, S. Takahashi, S. Mitani, and M. Hayashi, The spin Nernst effect in tungsten, Sci. Adv. **3**, e1701503 (2017).

[65] Y. Pu, D. Chiba, F. Matsukura, H. Ohno, and J. Shi, Mott Relation for Anomalous Hall and Nernst Effects in $Ga_{1-x}Mn_xAs$ Ferromagnetic Semiconductors, Phys. Rev. Lett. **101**, 117208 (2008).

[66] G. Kresse and J. Hafner, *Ab initio* molecular dynamics for liquid metals, Phys. Rev. B **47**, 558 (1993).

[67] G. Kresse and J. Furthmüller, Efficiency of *ab-initio* total energy calculations for metals and semiconductors using a plane-wave basis set, Comput. Mater. Sci. **6**, 15 (1996).

[68] G. Kresse and J. Furthmüller, Efficient iterative schemes for *ab initio* total-energy calculations using a plane-wave basis set, Phys. Rev. B **54**, 11169 (1996).

[69] A. A. Mostofi, J. R. Yates, Y.-S. Lee, I. Souza, D. Vanderbilt, and N. Marzari, Wannier90: A tool for obtaining maximally-localised Wannier functions, Comput. Phys. Commun. **178**, 685 (2008).

[70] Q. Wu, S. Zhang, H.-F. Song, M. Troyer, and A. A. Soluyanov, Wanniertools: An open-source software package for novel topological materials, Comput. Phys. Commun. **224**, 405 (2018).

[71] G. Kresse and D. Joubert, From ultrasoft pseudopotentials to the projector augmented-wave method, Phys. Rev. B **59**, 1758 (1999).